Elasticity and fracture of brick and mortar materials using discrete element simulations

Kaoutar Radi, David Jauffrès, Sylvain Deville, Christophe L. Martin

Printed in Journal of the Mechanics and Physics of Solids, Elsevier, 2019, 126, pp.101-116. 10.1016/j.jmps.2019.02.009.

Elasticity and fracture of brick and mortar materials using discrete element simulations

Kaoutar Radi[a], David Jauffres[a], Sylvain Deville[b], Christophe L. Martin[a]

[a] *Univ. Grenoble Alpes, CNRS, Grenoble INP, SIMaP, F-38000 Grenoble, France*
[b] *Laboratoire de Synthèse et Fonctionnalisation des Céramiques, UMR 3080 CNRS/Saint-Gobain CREE, Saint-Gobain Research Provence, Cavaillon, France*

Abstract

Natural materials such as bone and the nacre of some seashells are made of relatively weak building blocks and yet often exhibit remarkable combinations of stiffness, strength, and toughness. Such performances are due in large part to their brick and mortar architectures. Many efforts are devoted to translate these design principles into synthetic materials. However, much of the progress is based on trial-and-error approaches, which are time consuming and do not guarantee that an optimum is achieved. Modeling is an appealing alternative to guide the design and processing routes of such materials. However, the current analytical approaches cannot describe the extrinsic toughening mechanisms that takes place during crack propagation and are responsible for the remarkable properties of such materials. Here we show that the Discrete Element Method (DEM) can be used to predict the elastic and fracture behavior of brick and mortar materials and capture non-continuous phenomena such as multi-cracking. In contrast with most analytical shear-lag models, which only predict crack initiation, the model proposed here can also tackle crack propagation. DEM simulations are compared to analytical results with special attention to the shear transfer at the interface. The case of nacre-like alumina–a ceramic/ceramic brick and mortar composite with a brittle interface–is investigated to illustrate the potential of the method. We demonstrate in particular the importance of controlling the interface strength for further optimization of the mechanical properties. This method could be extended to predict and investigate the behavior of brick and mortar composites with a ductile interface, such as polymer/ceramic or metal/ceramic composites.

Keywords: Discrete Element Method, Brick and mortar materials, Elasticity, Fracture, Bio-inspired materials, Nacre.

Email address: christophe.martin@grenoble-inp.fr (Christophe L. Martin)

1. Introduction

Structural biological materials often exhibit impressive mechanical properties, such as unique combinations of strength and toughness (Chen et al. [2008]). Nacre, that covers the inside of many seashells species, is a composite which toughness is several orders of magnitude larger than its constituents. Nacre is primarily a hierarchical composite with a brick and mortar (BM) architecture : aligned mineral tablets (bricks) are linked together by a thin organic interface (mortar) providing cohesion and energy dissipation capacity to the material (Jackson et al. [1988], Espinosa et al. [2009]). The architecture of nacre also includes many other structural features defined at different length scales, from the fibril network of the interface to the arrangement of mesolayers (Barthelat et al. [2016]). The high performances of nacre can be attributed to this hierarchical architecture.

Various processing routes have been developed (mainly in the last decade) to produce synthetic BM materials inspired by the structure of nacre (Corni et al. [2012], Zhao and Guo [2017]). A common belief is that some ductility is required at the interface for an efficient toughening of the composite, directing thus research almost exclusively towards ceramic/polymer and ceramic/metal composites. A resulting drawback is the inability of these BM composites to sustain harsh environment conditions (high-temperature or oxidative), as well as a moderate strength. Thus, there is still a lack of damage-resistant refractory materials, which current composites cannot fulfill satisfactorily.

Recently, a new bioinspired BM material, nacre-like alumina, has been developed (Bouville et al. [2014]). In contrast with metal-ceramic or polymer-ceramic composites, this ceramic-ceramic composite can maintain high strength and high toughness at 600°C and keep good oxidation properties. The material is composed of brittle constituents only : 98.5 vol.% of alumina platelets, 1.3 vol.% of silica, and 0.2 vol.% of calcia. In the absence of a ductile interface, the reinforcement mechanisms responsible for the high toughness include microcracking, crack deviation, and crack bridging (Bouville et al. [2014]). The incorporation of alumina nanoparticles at the interface plays an essential role by forming nano-bridges between the platelets and nano-asperities at their surface, providing thus energy dissipation mechanisms during crack propagation by platelet pull-out, bridge breakages, and sliding friction (Grossman et al. [2017]). The extrinsic nature of the reinforcement mechanisms is confirmed by a R-curve behavior (Bouville et al. [2014], Launey and Ritchie [2009]). Further work has extended the compositions (Pelissari et al. [2018]) and processing routes (Le Ferrand et al. [2015, 2018]) of such materials.

The work by Bouville et al. [2014] demonstrates the possibility, using only ceramics constituents, of engineering BM materials with a sufficiently high toughness to avoid catastrophic failure. A good understanding of the reinforcing mechanisms and appropriate modeling is nonetheless necessary to optimize the material microstructure in terms of platelets aspect ratio, interface thickness and interface strength. Such an optimization can for example be achieved by a change in composition, or the fine tuning of the amount of nano-bridges.

Modeling the mechanical properties of BM material has been mainly approached by analytical shear-lag models, where the load transfer between tablets is studied at

the scale of a Representative Volume Element (RVE). These models come with necessary simplifications which limit their applicability. A common assumption, used for example by (Barthelat [2014], Zhang et al. [2010], is that shear stress is uniform within the interface, which implies a much stiffer tablet than the interface. This is a reasonable assumption for the natural or synthetic nacres with a polymeric interface but an all-ceramic BM material has a stiffness ratio (interface/tablet) close to unity. Only a few sophisticated models have been developed to account for non-uniform shear and can be applied to composites with a stiffness ratio close to unity (Begley et al. [2012a], Ni et al. [2015]).

In addition, the majority of analytical models are elasto-plastic and focus only on stiffness, strength, and energy adsorption at the onset of crack propagation. Extrinsic toughening mechanisms that are predominant for nacre-like composite ceramics during crack propagation, are difficult to capture by this class of analytical models. Sun et al. [2015] have proposed a model for bioinspired carbon nanotube bundles to account for the gradual loss in modulus and strength as the crack propagates. Song et al. [2016] have used a non-linear shear-lag model to study the progressive failure of interfaces on a laminate with a dozen tablets. As an attempt to model a specific extrinsic mechanism, crack bridging, an interfacial cohesive law has been proposed using analytical approaches (Shao et al. [2012], Barthelat and Rabiei [2011]).

Useful design guidelines and property maps have been derived from these models, and show that optimal combinations of platelet aspect ratio, interface thickness, and yield stress that maximize composite strength and toughness exist (Begley et al. [2012b], Barthelat [2014], Ni et al. [2015]). For example, for a given geometry, increasing the interface yield stress will be beneficial up to the point where the failure mechanism will shift from interface yield to brick failure, thus leading to an optimal interface yield stress (Begley et al. [2012b]).

Numerical modeling approaches could potentially capture crack propagation and R-curves, i.e. extrinsic toughening mechanisms. FEM has been scarcely used probably due to difficulties to handle topological modifications and a large number of tablets (Bekah et al. [2012], Katti et al. [2005]). Preferred options include discrete methods based on shear-lag description of tablet interactions (William Pro et al. [2015], Abid et al. [2018]) or spring lattice models (Sen and Buehler [2011]). The Discrete Element Method (DEM) based on spherical discrete elements originally designed for granular materials (Cundall and Strack [1979], Dubois and Radjai [2011], Chareyre [2019]) has probably never been used for BM materials but was successfully used on a layered structure–albeit only in 2D–by Zhang et al. [2014]. DEM can naturally account for multiple cracking and frictional contacts between the newly created surfaces and thus provide the required ingredients for the explicit modeling of extrinsic reinforcements (Jauffrès et al. [2012], Roussel et al. [2016]). In addition, there is no need to predefine (for mesh refinement purpose for example) the location of the crack path.

The application of DEM to dense materials implies a careful calibration of contact laws to reproduce the macroscopic elastic and fracture behavior André et al. [2012, 2013], Kumar et al. [2016], Leclerc et al. [2017]). It is particularly well-suited to model composite materials made of elastic-brittle phases (Maheo et al. [2015]).

The present work focuses on the development and validation of DEM simulations for nacre-like ceramics made of elastic brittle constituents but is generic enough to be

applicable to all BM materials. The DEM contact laws and the calibration procedure are first described. The mechanical response of a BM RVE is then carefully studied and compared to existing analytical shear-lag models. The capacity of this modeling approach to capture damage and crack propagation is highlighted. Finally, as an application example of the model, the optimization of the interface strength of nacre-like alumina is presented.

2. Modeling of a continuous material with DEM

2.1. Microscopic beam model

The mechanical behavior of a continuous material is modeled by a network of beams connecting spherical particles of radius R (Fig. 1). For two particles (labeled 1 and 2), with radii R_1 and R_2, the effective radius R^* is defined as :

$$R^* = \left(\frac{1}{R_1} + \frac{1}{R_2}\right)^{-1} \tag{1}$$

Similarly, a bond between two particles with normal and tangential stiffnesses K_N and K_T carries effective stiffnesses :

$$K_N^* = \left(\frac{1}{K_{N,1}} + \frac{1}{K_{N,2}}\right)^{-1}, \quad K_T^* = \left(\frac{1}{K_{T,1}} + \frac{1}{K_{T,2}}\right)^{-1} \tag{2}$$

The normal and tangential stiffnesses K_N^* and K_T^* introduce a size dependence in the model. Thus, we prefer using material parameters $\sigma_N^* = \frac{K_N^*}{2R^*}$ and $\sigma_T^* = \frac{K_T^*}{2R^*}$, which have the unit of stress and allow macroscopic elastic properties to be independent of the sphere size for a given set of microscopic properties σ_N^* and σ_T^*. The normal and tangential forces at the bond scale are thus given by :

$$\mathbf{N} = -4\sigma_N^* R^* \delta_N \mathbf{n} \tag{3}$$

$$\mathbf{T} = -4\sigma_T^* R^* \delta_T \mathbf{t} \tag{4}$$

where δ_N and δ_T are the normal and the tangential relative displacements between the two particles, and $\mathbf{n}$ and $\mathbf{t}$ are the unit normal and tangential vectors, respectively.

The normal force $\mathbf{N}$ may be attractive or repulsive. Bonds transmit resisting moments M_N and M_T in the normal and tangential directions that oppose the accumulated relative rotations θ_N and θ_T (Potyondy and Cundall [2004]) :

$$M_N = -8\sigma_T^* R^{*3} \theta_N \tag{5}$$

$$M_T = -4\sigma_N^* R^{*3} \theta_T \tag{6}$$

Note that the formulation in Eqs. (5) and (6) assumes that the radius of the cylindrical beam bonding the two particles is equal to twice the equivalent radius R^* (Potyondy and Cundall [2004], Kumar et al. [2016]).

The beam model described above associated with the Discrete Element Method (DEM) Cundall and Strack [1979] allows the elastic behavior of a continuous material to be represented satisfactorily ([Kumar et al., 2016]). In particular, the Poisson effect can be reproduced, although within a limited range of value of the Poisson's ratio ($-0.4 \leq \nu \leq 0.35$). Also, we have shown that the simple bond model proposed here is capable of simulating elastic instabilities such as buckling, without any built-in buckling mechanism artificially introduced in the model (Kumar et al. [2016]).

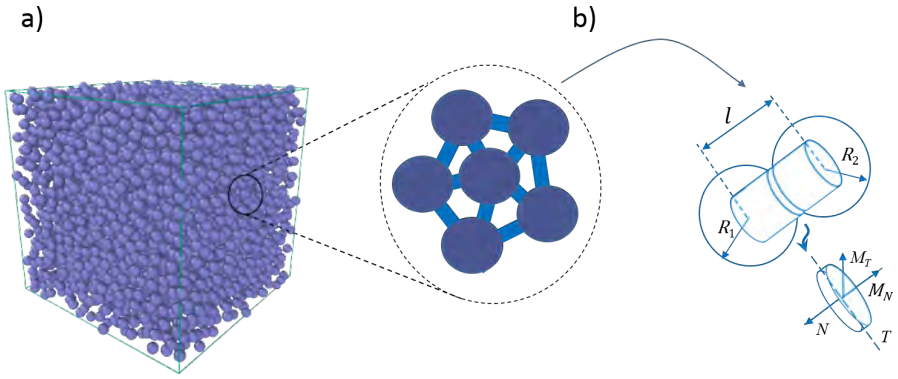

FIGURE 1: From macroscopic to microscopic scale. (a) Random packing of bonded particles representing a continuous material. (b) Two bonded particles of radius R_1 and R_2 transmitting normal/tangential forces and resisting moments.

2.2. *Fracture criterion*

The inherent discrete nature of the DEM description of a material provides a natural framework to deal with fracture. Two major approaches exist to model fracture. The first one is based on the simple deletion of a particle when a fracture criterion is satisfied by the stress tensor computed at the particle scale (André et al. [2013], Maheo et al. [2015], Leclerc et al. [2016]). The drawback is that volume conservation is not ensured and that complex strain paths that may lead to crack closure cannot be correctly modeled. The second method, adopted here, consists of the evaluation of the stress (or the strain) within the bond, and the application of a critical stress/strain criterion at the bond level (Potyondy and Cundall [2004], Carmona et al. [2008]). Once the bond has reached the criterion, the particles and the bond are kept but the bond behavior is modified as detailed below. The criterion typically involves normal and/or tangent stresses or a combination of both.

In this work we use the Rankine maximum principal stress criterion at the scale of a beam, which is suitable for predicting failure in brittle materials. Rankine criterion states that failure occurs when the maximum principal stress reaches either the uniaxial tension strength, or the uniaxial compression strength. For the beam model, Rankine's equivalent stress is :

$$\sigma_{b,R} = \frac{1}{2}\left(\sigma_{b,N} + \sqrt{\sigma_{b,N}^2 + 4\sigma_{b,T}^2}\right) \tag{7}$$

where $\sigma_{b,N} = \frac{N}{4\pi R^{*2}}$ and $\sigma_{b,T} = \frac{T}{4\pi R^{*2}}$ are the normal and the tangential stresses at

the bond scale. The bond breaks when the Rankine's equivalent stress $\sigma_{b,R}$ reaches a critical stress σ_{Rc}. As demonstrated by André et al. [2013] this approach may not be relevant for complex triaxial loading such as indentation. However, it should be suitable for the case of BM materials under tensile loading where mainly stress states close to pure tension or pure shear are encountered.

After bond fracture, DEM provides a simple mean to model crack closure if particles resume contact (or if the bond fractured in shear while under compressive stresses, $\sigma_{b,N} < 0$ in Eq. (7)). This is accomplished by stating that a broken bond keeps the same normal stiffness as an unbroken bond in compression but cannot transmit any tensile force. The tangential forces transmitted by broken bonds follow the Hertz–Mindlin model in the sticking mode and are limited by Coulomb friction for sliding (friction coefficient μ). Accordingly, broken bonds transmit only resisting moment M_T in the tangential direction but none in the normal direction (Fig. 2).

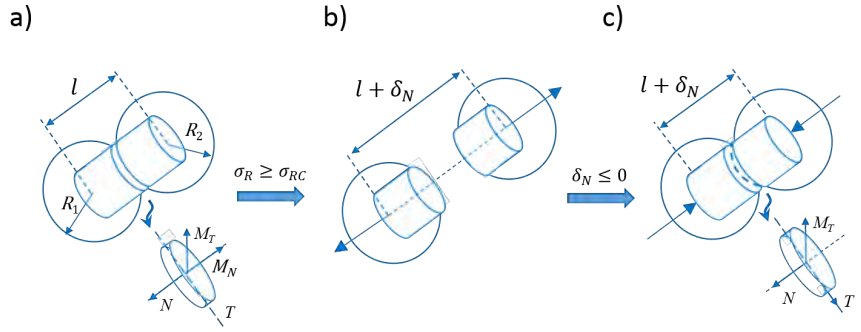

FIGURE 2: Two bonded particles transmitting normal/tangential forces and resisting moments. (a) Unbroken bond. (b) Broken bond. (c) Resumed contact after bond fracture transmitting only compressive forces, friction forces and tangential resisting moment.

2.3. DEM simulations

A classical dynamic DEM, as introduced by Cundall and Strack [1979], is used in a quasi-static approach within the in-house code dp3D (Martin et al. [2003]), to compute the equilibrium positions of particles at each time-step. The code is available for use on request. Strains are first imposed to the sample via periodic conditions or by the use of objects with infinite mass. Particles are displaced in the first half time-step according to the imposed increment in strain following the affine solution (homogeneous deformation of the sample). Contact forces (Eqs. (3) and (4)) are used to compute the total force acting on each particle. Newton's second law of motion enables the computation of the acceleration and an explicit time-integration scheme is used (velocity-Verlet) to obtain the new position of the particles before a new strain increment is imposed. New contacts and lost contacts are updated at each time-step.

Small enough time-steps and slow enough strain rates are employed to ensure stability and quasi-static equilibrium. More details relative to these aspects can be found in a previous publication (Martin et al. [2003]). Concerning quasi-static conditions, the value of the imposed strain-rate is set at each time-step with consideration to the

normalized kinetic energy per particle (Agnolin and Roux [2007]) :

$$\tilde{E}_{kin} = \frac{E_{kin}}{n \max(NR^*)} \tag{8}$$

where E_{kin} is the total kinetic energy of the particle system (accounting for rotation and translation terms), n the number of particles and N the normal force (Eq. (3)). The strain-rate and the renormalized mass of particles are adapted so that $\tilde{E}_{kin}$ stays reasonably below 10^{-7} all along the simulation to ensure quasi-static conditions (Agnolin and Roux [2007]). Under such conditions, inertia effects are considered negligible. In particular, we have ensured that bond fracture events, which inevitably release some kinetic energy, do not induce detrimental inertia effects.

Under macroscopic strain, the network of beams, which microscopic interactions have been described above, transmit forces $\mathbf{F}$ at each bond resolved locally into a normal and a tangential component ($\mathbf{F} = \mathbf{N} + \mathbf{T}$). The macroscopic stress tensor resulting from these forces may be computed using Love's formulation (Christoffersen et al. [1981]) :

$$\Sigma_{ij} = \frac{1}{V} \sum_{beams} F_i l_j \tag{9}$$

where the summation is made on all (intact or broken) beams that transmit forces in the sample volume V, F_i is the i^{th} component of $\mathbf{F}$, and l_j is the j^{th} component of the branch vector l connecting the centers of two bonded particles (Fig. 1). A simple dimensional analysis shows that the use of the microscopic properties σ_N^* and σ_T^* to define material parameters leads, as it should, to a macroscopic response that is independent of the size of the particles that mesh the material.

2.4. Sample generation

Samples were generated using periodic conditions on all packings. A gas of nearly monomodal particles (5% dispersion around the average radius R) is first generated by locating particles randomly in a periodic cell. At this stage, particles have no contact and the relative density of the packing is approximately 0.3. By slowly moving inwards the periodic walls, the initial gas of particles is isostatically densified under Hertzian contact law (Martin and Bordia [2008]) (no bonds nor any friction or adhesion between particles during this preparation stage) until a density $D = 0.5$ is obtained. Following the work by Kumar et al. [2016], we further densify the packing by imposing an affine densification until a final density $D = 0.65$ is reached. This procedure is identical to the so called "weakly jammed" preparation route used by Kumar et al. [2016].

At this stage, all pairs of particles that are close enough are bonded together to form a continuous material according to the following criteria :

$$\kappa(R_1 + R_2) \geq | \mathbf{l}_{12} | \tag{10}$$

where $\mathbf{l}_{12}$ is the branch vector between the center of the pair of particles (Eq. (9) and Fig. 2) and κ is the interaction range. In our case, the interaction range $\kappa = 1.075$ provides enough interlocking between particles as proposed by Jerier and Molinari [2012], Scholtès and Donzé [2013]. We tested previously (Kumar et al. [2016]) that this value allows Poisson's ratios in the [0–0.35] range to be simulated.

In short, a numerical sample is thus meshed with a network of bonds and particles as described above. It is characterized by a particles number n, a relative density D and an average bond number Z_b per particle. Fig. 3 summarizes the sample preparation in which a particles gas is densified to form a random packing of particles bonded together.

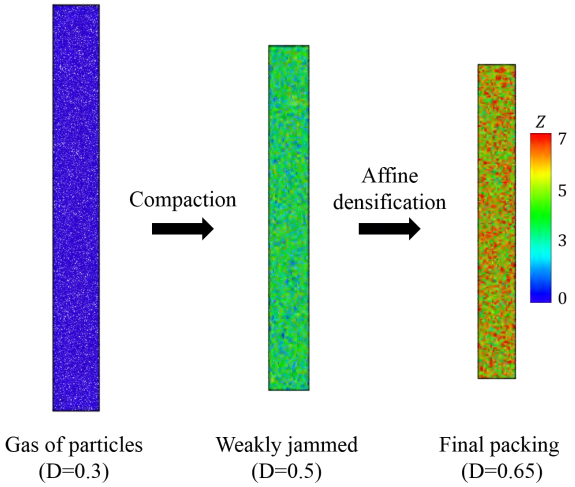

FIGURE 3: Typical evolution of a numerical 3D sample with 20 000 particles during the preparation stage. (a) The initial gas of particles has no contact between particles ($Z = 0$) and a relative density $D = 0.3$. (b) The weakly jammed packing is characterized by an average coordination number $Z = 3.58 \pm 0.02$ and a relative density $D = 0.5$. (c) A final affine densification is imposed ($D = 0.65 \pm 0.01$ relative density) and bonds are installed ($Z_b = 6.65 \pm 0.02$) with an interaction range $\kappa = 1.075$ (Eq. (10).

2.5. Elasticity and strength calibration

When using a random packing in DEM to model a continuous material, the relationship between the microscopic interaction laws (bond level) and the macroscopic response (the discrete sample level), cannot be reached analytically. Thus, a calibration process is required to determine the appropriate microscopic parameters that reproduce the material macroscopic behavior (Potyondy and Cundall [2004], André et al. [2012]).

Moreover, the macroscopic behavior depends on the geometrical arrangement of the discrete network of bonds. To calibrate the microscopic parameters in the contact laws, we rely on the work of Kumar et al. [2016] who performed extensive quasi-static tensile tests in order to establish relationships between the macroscopic elastic behavior of the packing and the contact stiffnesses for various packing preparations routes. Based on a generalization of the mean field solution, they proposed simple calibration equations to relate the macroscopic elastic response of the packing (the Young's modulus E and the Poisson's ratio ν) to the packing characteristics (Z_b and D), and to the microscopic parameters at the bond scale (σ_N and σ_T). For the simple case of a packing of particles with identical microscopic parameters σ_N and σ_T ($K_{N,1} = K_{N,2}$

and $K_{T,1} = K_{T,2}$ in Eq. (2)), these equations write :

$$\sigma_N = \frac{E}{Z_b D} \frac{2\pi}{\kappa^m} \frac{4 + a_3\alpha}{a_1 + a_2\alpha} \tag{11}$$

$$\sigma_T = \alpha\sigma_N \tag{12}$$

with :

$$\alpha = \frac{1 - b_2\nu}{b_1 + b_3\nu} \tag{13}$$

where κ is the interaction range (Eq. (10)) and m, a_i and b_i are fitted parameters ($m = 2$, $a_1 = 0.42$, $a_2 = 7.45$, $a_3 = 8.68$, $b_1 = 0.55$; $b_2 = 3.02$; $b_3 = 5.75$) for the weakly jammed preparation route (Kumar et al. [2016]). In the next sections we consider that the bricks/tablets and the mortar/interface have different Young moduli but identical Poisson's ratios, $\nu = 0.2$, typical of ceramics.

Rewriting Eq. (11), we define a normalized macroscopic Young's modulus $\tilde{E}$:

$$\tilde{E} = \frac{E}{\sigma_N} = Z_b D \frac{\kappa^m}{2\pi} \frac{a_1 + a_2\alpha}{4 + a_3\alpha} \tag{14}$$

which shows, together with Eq. (13) that the macroscopic elastic parameters not only depend on the normal and tangential stiffnesses of the bond network but also on the relative density D and on the average bond number Z_b of the particle packing that has been used to construct this network.

Similarly, one may expect that the macroscopic strength Σ of the material defined by the bond network should also depend on D and Z_b. Considering the dependence of the macroscopic elastic behavior on particles arrangement parameters, we thus computed the macroscopic strength for the weakly jammed preparation route.

Five sets of samples with various (Z_b, D) values having a $165R$x$16.5R$x$16.5R$ size in the x, y and z directions, respectively, were generated. For each set, five samples were generated with different initial random seeds. The particles number $n = 7\ 000$ was chosen large enough to ensure that the convergence of the measured macroscopic property (elastic modulus or strength) is reached (Kumar et al. [2016]). Tensile tests were carried out with periodic conditions and shear tests were carried out with non periodic conditions. Tensile loading was applied in the x direction while xy pure shear was obtained by enforcing $\sigma_{yy} = 0$ during the computation.

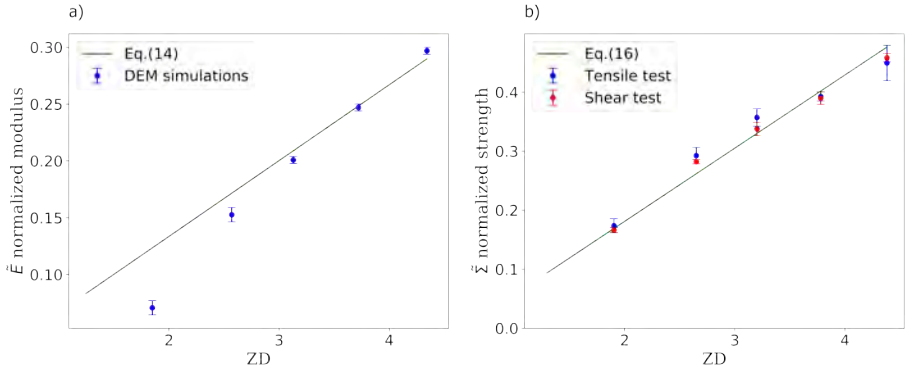

FIGURE 4: Calibration of macroscopic properties of the RVE : (a) Normalized Young's modulus $\tilde{E} = \frac{E}{\sigma_N}$ and Eq. (14). (b) Normalized strength $\tilde{\Sigma} = \frac{\Sigma}{\sigma_R}$ calibrated in tensile and shear tests.

The stress strain curves obtained from the tensile and pure shear tests exhibit a linear behavior followed by brittle fracture. Both elastic constants (E,ν) and strength can be extracted from these simulations. Fig. 4a shows the DEM simulation results for the normalized Young's modulus $\tilde{E}$ (Eq. (14)) versus the product Z_bD. The agreement with Eq. (14) is reasonable for $Z_bD > 3$.

Fig. 4b shows the evolution of the macroscopic strength for different values of the Z_bD product. Similarly to elasticity (Fig. 4a), Fig. 4b confirms the influence of the packing parameters on the macroscopic strength. After fitting the strength results from tensile and shear tests, a simple common transition law between microscopic and macroscopic strength can be obtained :

$$\tilde{\Sigma} = c_1 Z_b D - c_2 \tag{15}$$

where $\tilde{\Sigma} = \frac{\Sigma}{\sigma_{Rc}}$ is the normalized macroscopic strength and $c_1 = 0.124$; $c_2 = 0.067$ are fitted parameters. Eq. (15) together with Eqs. (13) and (14) cannot be considered as calibration equations per se and should only be considered as an approximate tool to compute macroscopic properties from microscopic bond parameters. For small values of the Z_bD product, it is clear that DEM simulations lead to a smaller normalized Young's modulus than predicted by Eqs. (13) and (14) as the percolation threshold is approached. Thus, the simple relation proposed by Kumar et al. [2016] should only be considered as a rough guideline for choosing elastic microscopic parameters in the domain $Z_bD > 3$. In the following, packings characterized by a product $Z_bD = 4.34$ have been used to mesh BM materials. In that case, the following calibration corresponding to our simulations (Fig. 4) has been taken for the microscopic parameters :

$$\sigma_N = 3.33E \tag{16}$$

$$\sigma_{Rc} = 2.12\Sigma \tag{17}$$

3. Modeling a brick and mortar material

3.1. Representative Volume Element (RVE)

To capture the mechanical behavior of the BM material, we set a 2D periodic Representative Volume Element composed of two tablets and two interfaces. This RVE is classically used in the literature for the development of analytical solutions (Barthelat [2014], Begley et al. [2012b] and finite element simulations (Bekah et al. [2012]). Fig. 5 shows a typical periodic configuration of the RVE, discretized with DEM particles. Tablets are connected horizontally by thin (red) interfaces and are separated vertically from each other by free surfaces. Such a model has the advantage of being sufficiently simple to allow for elegant analytical solutions (Barthelat [2014]) while capturing the load transfer from tension in the tablets to shear at the interface.

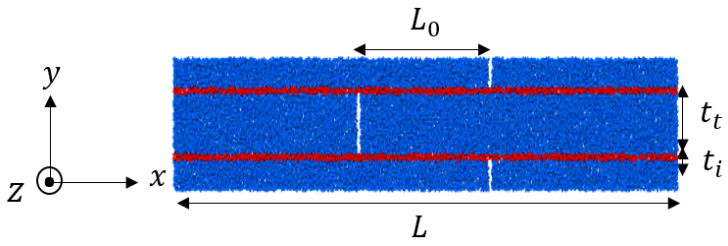

FIGURE 5: Representative Volume Element generated with discrete particles. Red particles mesh interfaces and blue particles mesh tablets. L, L_0, t and t_i are geometrical parameters characterizing the RVE.

Using the RVE microstructural parameters and the geometrical parameters specified in Fig. 5, we define in accordance with the notations in Barthelat [2014], the tablet volume fraction ϕ :

$$\phi = \frac{t_t}{t_t + t_i} \tag{18}$$

the tablet aspect ratio ρ :

$$\rho = \frac{L}{t_t} \tag{19}$$

the overlap aspect ratio ρ_0 :

$$\rho_0 = \frac{L_0}{t_t} \tag{20}$$

and the overlap ratio k :

$$k = \frac{L_0}{L} = \frac{\rho_0}{\rho} \quad \text{with} \quad 0 < k \leq 0.5 \tag{21}$$

where subscripts i and t stand for interface and tablet, respectively. For the sake of comparison with existing analytical models (Barthelat [2014]), the vertical interfaces are not filled by DEM particles which means that no stress is carried in the x direction

between two tablets. 3D DEM simulations are run in a pseudo 2D configuration with 4 ± 1 particles in the thickness and periodic boundary conditions in all three directions, with $\epsilon_{zz} = 0$ to ensure plane strain conditions.

In the DEM unit cell shown in Fig. 5, each phase is represented by a given particle type assigned with microscopic parameters to model its mechanical behavior. These parameters are calibrated independently for the tablet and the interface as described in section 2.5.

The stiffness of bonds between interface and tablets particles are treated in series (Eq. (2)). As for fracture, the critical Rankine strength of interface-tablet bonds is dictated by the smallest strength of the interface-interface and tablet-tablet bonds.

3.2. Homogenization procedure

To investigate the anisotropic behavior of brick and mortar materials, we performed tensile loadings in both axial and transverse direction. For the axial loading the numerical sample is subjected a macroscopic strain ϵ_{xx} and periodic boundary conditions ($\epsilon_{yy} = 0$) and conversely for the transverse loading. Due to the material's microstructure, the effective elastic tensor is orthotropic (Bertoldi et al. [2008]). In a plane strain configuration the axial and transverse modulus are computed as follows :

$$\tilde{E_x} = \frac{E_x}{E_t} = \frac{1}{E_t}\frac{1}{\epsilon_{xx}}\left(\Sigma_{xx}^{axial} - \left(\frac{\Sigma_{xx}^{transv}}{\Sigma_{yy}^{transv}}\right)\Sigma_{yy}^{axial}\right) \tag{22}$$

$$\tilde{E_y} = \frac{E_y}{E_t} = \frac{1}{E_t}\frac{1}{\epsilon_{yy}}\left(\Sigma_{yy}^{transv} - \left(\frac{\Sigma_{yy}^{axial}}{\Sigma_{xx}^{axial}}\right)\Sigma_{xx}^{transv}\right) \tag{23}$$

where *axial* and *transv* stand for axial and transverse loadings, respectively.

3.3. Convergence study

We generated thirteen different three-dimensional RVEs with different particles number n to define the minimum number of particles that allows stable macroscopic properties to be obtained with a periodic RVE. More generally, we study in this section the influence of mesh refinement on elastic and fracture properties. For each discrete set with a given number of particle n, five initial samples were generated using different random seeds to compute standard deviations. Each set of particles was generated as described in section 2.4. The tablet aspect ratio is $\rho = 16$, the overlap ratio $k = 0.5$ and a tablet volume fraction $\phi = 0.87$. All samples exhibit a size ratio of $80 \times 10 \times 1$ in the three directions. The packing characteristics and the input parameters are reported in table1.

Packing characteristics		Input parameters		
κ	ZD_b	α	$\frac{\sigma_N}{E}$	$\frac{\sigma_{RC}}{\Sigma}$
1.075	4.34	0.21	3.33	2.12

TABLE 1: Packing characteristics and input parameters used in the simulations. σ_N and σ_{RC} are normalized by the macroscopic Young's modulus E and the macroscopic strength σ, respectively.

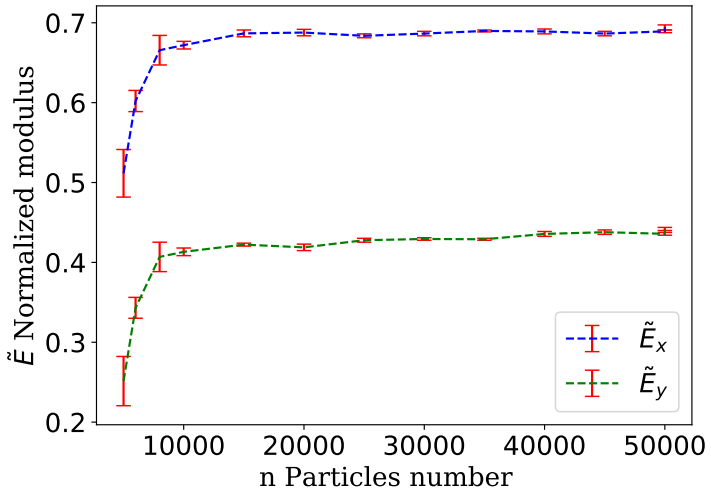

FIGURE 6: Evolution of macroscopic normalized moduli $\tilde{E}_x$ and $\tilde{E}_y$ for the RVE shown in Fig. 5 against the particle number n for a constant set of microscopic parameters. Sample characteristics : tablet aspect ratio $\rho = 16$, overlap ratio $k = 0.5$, and $\phi = 0.87$.

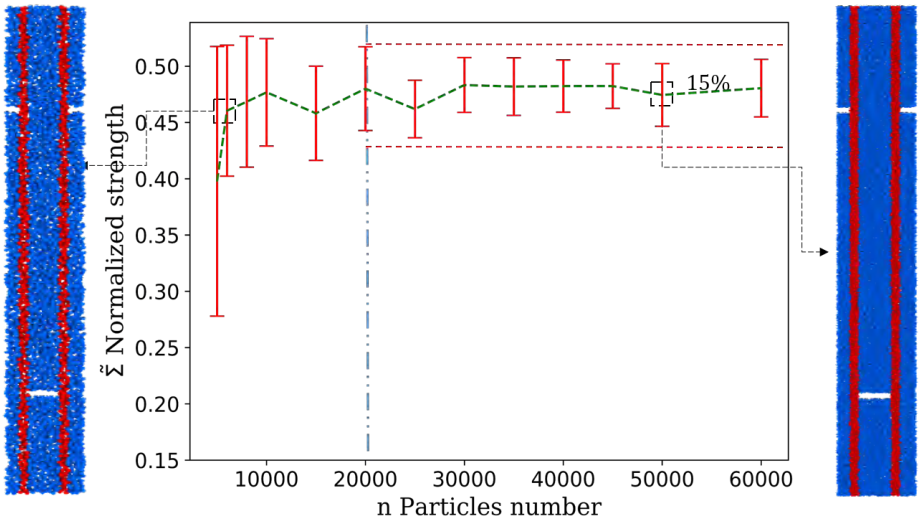

FIGURE 7: Evolution of macroscopic normalized strength $\tilde{\Sigma}$ against particle number n for a constant set of microscopic parameters.

Figures 6 and 7 show the convergence of the elastic moduli and strength as the particle number increases. For a particle number larger than 10 000, the Young's modulus clearly converges with a low standard deviation, which seems inherent to the random discrete nature of the packing used to mesh the RVE. Concerning strength, convergence can be considered satisfactory for $n \geq 10\,000$. Hereafter samples are generated with 20 000 particles to ensure that the thinner part of the material (i.e. the interface) contains enough particles (we observed that four particles are sufficient with periodic boundary conditions) to obtain convergence even with a slightly larger tablet volume fractions ϕ.

Interestingly, Fig. 6 demonstrates that the RVE exhibits a clear anisotropic elastic response. The axial Young's modulus (E_x) is nearly twice as large as the transverse modulus (E_y). This is generally ignored by analytical models that only consider the axial behavior of the RVE.

4. Comparison with analytical models

4.1. Elastic modulus

Assuming that there is no vertical interface, i.e. no load transfer in tension between tablets, the classical shear-lag model (Barthelat [2014], Ni et al. [2015], Ji and Gao [2004], Begley et al. [2012b]) leads to the RVE Young's modulus as a function of the Young's modulus of the tablet and the interface. Barthelat [2014] proposed :

$$\tilde{E}_x = \frac{E_x}{E_t} = \frac{\phi}{1 + \frac{1}{\beta}\left(\coth(k\beta) + \coth(\beta(1-k)\right)} \quad \text{with} \quad \beta = \rho\sqrt{\frac{1}{2(1+\nu)}\frac{E_i}{E_t}\frac{\phi}{1-\phi}} \tag{24}$$

Ni et al. [2015] and Begley et al. [2012b] proposed :

$$\tilde{E}_x = \frac{E_x}{E_t} = \frac{2\beta \sinh\left[(1-k)\beta\right] \sinh(k\beta)}{2\sinh(\beta) + \beta\left[\cosh(\beta) - \cosh\left((2k-1)\beta\right)\right]} \tag{25}$$

and Ji and Gao [2004] proposed :

$$\tilde{E}_x = \frac{E_x}{E_t} = \frac{1}{\left(1 + \frac{1-\phi}{\phi}\right)\left(1 + \frac{8}{\rho^2}\frac{1-\phi}{\phi}(1+\nu)\right)} \tag{26}$$

where ϕ, ρ, and k are geometrical parameters defined in Eqs. (18), (19), and (21), respectively. The form of Eqs. (24) and (25) proposed by their authors are reproduced here but one may notice that an analytical simplification of Eq. (25) demonstrates that the two models only differ by a factor of ϕ. Note that the model of Ni et al. [2015] (Eq. (25)) is only valid for sufficiently large values of the tablet volume fraction (typically $\phi > 0.8$). Also, the model of Ji and Gao [2004] has been developed only for a symmetric overlap ($k = 0.5$).

FIGURE 8: Normalized macroscopic Young's modulus $\frac{E_x}{E_t}$ from DEM simulations (bullet symbols) as a function of the overlap aspect ratio for three different tablet volume fractions ϕ with an aspect ratio $\rho = 20$, and a 0.1 Young's modulus ratio ($E_i/E_t = 0.1$). DEM simulation results are compared to three analytical models Eqs. (24), (25), (26) ($\rho_0 = k\rho$)(Eq. (21)). Eq. (26) is valid only for a symmetric overlap (i.e. $\rho_0 = 10$). Standard deviations are calculated based on five simulations.

By varying k for $\rho = 20$, Fig. 8 shows the evolution of the normalized Young's modulus $\frac{E_x}{E_t}$ against the overlap aspect ratio ρ_0, which is the parameter controlling the elastic modulus and encompassing both the effects of ρ and k (Barthelat [2014]). Results for three different tablet volume fractions ϕ are compared to three analytical models (Begley et al. [2012b], Barthelat [2014], Ji and Gao [2004]). The numerical results were obtained for five realizations and E_x was calculated using the homogenization procedure described in section 3.2. The standard deviation on the normalized Young's modulus was around 4% for high volume tablet fraction showing limited influence of the initial packing arrangement.

A high tablet concentration leads to a high modulus and to less sensitivity to the overlap aspect ratio. Figure 8 shows that our simulation results are in good accordance with Barthelat's model. In particular, the region of stiff increase of the E_x/E_t ratio for small overlap aspect ratio is well rendered by this model. The model of Begley exhibits the same kind of transition, in agreement with our simulations, but overestimates the E_x/E_t ratio as compared to our DEM simulation results and Berthelat's model.

As indicated above (Fig. 6), the tested RVE exhibits an anisotropic elastic behavior. To validate the elastic modulus in the y direction, we compared it to the analytical model of Bertoldi et al. [2008], where E_y is given by :

$$\tilde{E}_y = \frac{E_y}{E_t} = \frac{[1 - \phi(1 - \frac{E_t}{E_i})](1-\nu^2)}{\Gamma} \tag{27}$$

where

$$\Gamma = \phi(1-\phi)(1+\nu)^2\left[(1-2\nu)(1+\frac{E_t^2}{E_i^2})+2\frac{E_t}{E_i}\nu^2\right]+\frac{E_t}{E_i}((1-\phi)^2+\phi^2)(1-\nu^2)^2 \quad (28)$$

Fig. 9 shows that in accordance with Fig. 8, Eq. (26) overestimates $\tilde{E}_x$ for $\phi \geq 0.5$. Note that analytical models are ill-suited for low tablet volume fractions ($\phi < 0.5$). More interestingly, the DEM simulated $\tilde{E}_y$ is compared to the above analytical model for increasing values of tablet volume fractions ϕ with a symmetric overlap ratio $k = 0.5$ and an overlap aspect ratio $\rho = 20$. $\tilde{E}_y$ values are in quite good agreement with the analytical model on the whole tablet volume fraction domain.

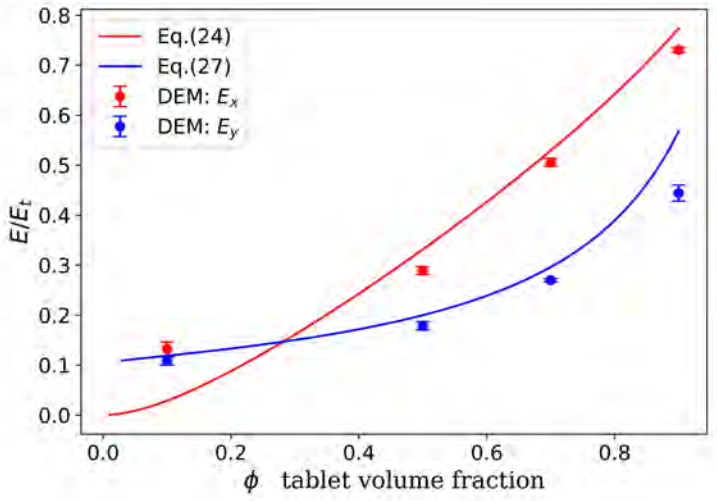

FIGURE 9: Normalized analytical Young's modulus $\tilde{E}_x$ and $\tilde{E}_y$ (Eqs. (26) and (27)) against the tablet volume fraction ϕ with an aspect ratio $\rho = 20$ compared to the DEM results (bullet symbols). The error bars are computed based on five simulations.

4.2. RVE failure

The analytical prediction of the strength of a brick and mortar arrangement has been tackled by numerous authors under various assumptions (Barthelat [2014], Ni et al. [2015], Begley et al. [2012b]). In particular, some authors considered the simplified case of uniform shear in the interface, which is a valid assumption for a large elastic modulus contrast ($E_i/E_t \ll 0.1$) between interface and tablet (or for an overlap aspect ratio close to unity, which is not of much engineering interest) (Barthelat [2014]). In that case, the normalized fracture initiation stress writes :

$$\tilde{\Sigma}_{init} = \frac{\Sigma_{init}}{\Sigma_t} = \min\left[\rho_0\phi\frac{\Sigma_i}{\Sigma_t}, \frac{1}{2}\right] \quad (29)$$

where Σ_t and Σ_i are tablet and interface strength, respectively. A critical overlap ratio, $(\rho_0)_c = \frac{\Sigma_t}{2\phi\Sigma_i}$ can be defined to point out when fracture initiation shifts from the

interface to the tablet. Note that the fracture initiation stress in Eq.(29) does not depend on $\frac{E_i}{E_t}$. The above model, valid for $\frac{E_i}{E_t} \ll 1$, is justified for biological materials or synthetic materials with a polymeric interface. A ceramic/glass or ceramic/ceramic brick and mortar structure will exhibit a markedly larger Young's modulus ratio (typically $\frac{E_i}{E_t} \geq 0.1$). In that case, the model developed by Begley et al. [2012b] and Ni et al. [2015] that accounts for non-uniform shear in the interface is more appropriate. It writes :

$$\tilde{\Sigma}_{init} = \frac{\Sigma_{init}}{\Sigma_t} = \min\left[\frac{\rho}{\beta}\frac{\Sigma_i}{\Sigma_t}\tanh(k\beta), \frac{1}{2}\right] \tag{30}$$

where β (see Eq. (24)) is a parameter that describes the magnitude of the shear transfer in the interface. The models accounting for uniform (Barthelat [2014]) and non-uniform shear transfer (Begley et al. [2012b], Ni et al. [2015] are very similar for $\frac{E_i}{E_t} \ll 1$.

To capture the brick and mortar behavior, we apply uniaxial tensile tests along the tablets under periodic conditions on nine RVE's with different overlap aspect ratios ρ_0 for $\rho = 10$, $\phi = 0.87$ and $\frac{\Sigma_t}{\Sigma_i} = 6$. For each RVE, five initial samples were generated using different random seeds to compute standard deviations. Fig. 10 shows a typical stress-strain curve. Two points are noteworthy on this curve. The stress Σ_{init} at which we consider that fracture initiates is chosen when 50 bonds are broken (or approximately 0.1% of the total number of bonds). This choice is rather arbitrary but consistent for all tests. Figure 10 indicates that this threshold corresponds to the end of a mild damage process that does not affect the linearity of the stress-strain curve, before large damage due to crack propagation that causes a change in slope on the stress-strain curve. The stress Σ_{max} simply defines the maximum stress attained by the sample. The difference between these two stresses gives us informations on the extrinsic mechanisms at play after crack initiation.

Figure 11a compares analytical models to DEM simulations for fracture initiation (Σ_{init} in Fig. 10). The accordance between models and DEM simulations is rather good. In particular, the stress plateau for $\rho_0 > (\rho_0)_c$ is well rendered. For $E_i/E_t = 10^{-3}$, this plateau corresponds to a fracture initiating in the tablets. For lower stiffness contrast, fracture always initiates in the interface due to larger stress concentration as shear transfer becomes less uniform in the interface Begley et al. [2012b], Ni et al. [2015].

As the crack propagation is not modeled in the analytical models (Begley et al. [2012b], Barthelat [2014], Ni et al. [2015]), the stress at crack initiation is considered equal to the maximum stress. However, initiation alone is not enough to characterize the fracture behavior of these brick and mortar materials. Fig. 11b shows that indeed when plotting the maximum stress (Σ_{max} in Fig. 10), the analytical models that predict only initiation differ markedly from our simulations. A clear difference between Fig. 11a and Fig. 11b is the the role of the stiffness ratio E_i/E_t. The stress at initiation is strongly linked to this ratio, while the maximum stress is weakly related to E_i/E_t (in particular for $E_i/E_t > 0.1$). For a large contrast of Young's modulus ($E_i/E_t = 10^{-3}$), the interface shear stress is uniform which results in very similar values for crack initiation and maximum stresses. However for a low modulus contrast ($E_i/E_t = 1$), the large stress concentration (non-uniform shear stress) leads to earlier crack initiation,

which explains the large difference between stress initiation and maximum stress. After crack initiation in the interface the crack propagates in a stable manner within the interface. Friction and interlocking effects build up rising stresses that ultimately can cause the crack to pass through the tablet leading to a catastrophic failure at approximately half the tablet strength. This explains why most of the data points in Fig. 11b fall on a plateau around $0.4\Sigma_t$. Only for low overlap aspect ratio and low stiffness contrast the crack is confined to the interface leading to a lower maximum stress value. We believe that interlocking effects inherent to DEM are realistic for brittle interfaces where newly created rough surfaces may interlock each other and resist to shear loading. The calibration of these mechanisms is possible through modifications of the packing characteristics and the friction law.

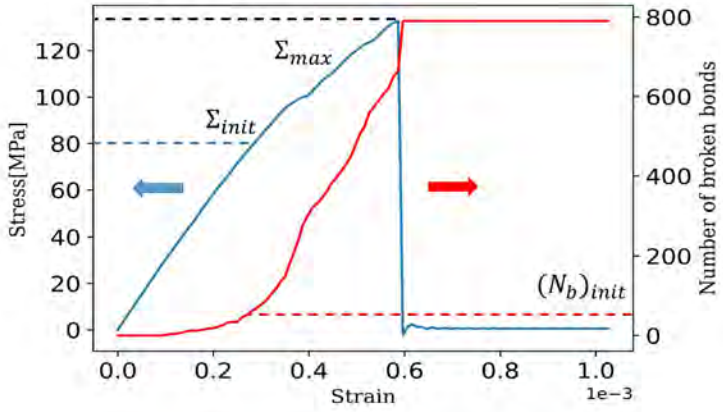

FIGURE 10: Typical stress-strain curve number of broken bonds from a DEM simulation for $\rho_0 = 2.5$ and $\frac{E_i}{E_t} = 0.1$. Two stresses are considered for comparison with analytical models. The fracture initiation stress Σ_{init} corresponds to the stress at which 50 bonds have broken. The strength Σ_{max} corresponds simply to the maximum axial stress.

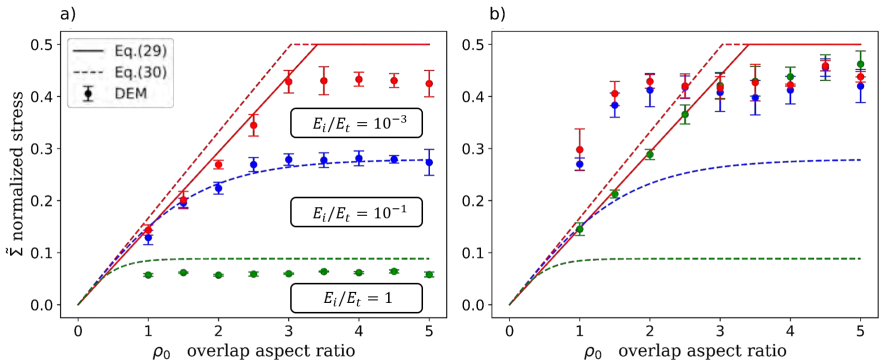

FIGURE 11: Normalized macroscopic stress $\tilde{\Sigma} = \frac{\Sigma}{\Sigma_t}$ of the RVE as a function of ρ_0 for three different stiffness ratios $\frac{E_i}{E_t}$ compared to analytical models (Ni et al. [2015], Barthelat [2014]. (a) Fracture initiation stress Σ_{init} and (b) Maximum stress Σ_{max} after crack propagation. Eq. (29) is only valid for small elastic modulus ratios for which it is very similar to Eq. (30).

5. Application to nacre-like alumina

To illustrate the potential of the numerical model developed in the previous sections, we apply it to nacre-like alumina. The model microstructural parameters mimic the material described by Bouville et al. [2014]. The tablets are made of alumina with a tablet volume fraction $\phi = 0.90$. The aspect ratio is $\rho = 14$, the overlap aspect ratio $\rho_0 = 3.5$ and the overlap ratio $k = 0.25$.

The mechanical properties are those of alumina (the tensile strength of tablets is $\Sigma_t = 5.3$ GPa, Feilden et al. [2017]). In our case, we consider a tablet/interface stiffness ratio of 0.1. The interface strength Σ_i is left as a parameter as it is the main material parameter that can be tuned experimentally (through composition, residual porosity, ...). To investigate its influence and more generally the influence of the strength ratio between interface and tablet, we generated several samples with interface strengths smaller than the strength of the alumina tablets ($\Sigma_i = [50, 4000]$ MPa).

By applying uniaxial tensile loading as in section 3, we obtain stress-strain curves as illustrated in Fig. 12. Using the stress/strain curves of each sample, and the number of broken bonds per particle (Fig. 13) of three different samples ($\Sigma_i = 200$; 1 300, 4 000 MPa), three failure behaviors can be distinguished (Fig. 14) :

- Crack initiation and propagation in the interface (regime 1) for low values of Σ_i.
- Crack initiation at the interface and propagation in the tablet (regime 2) for intermediate values of Σ_i.
- Crack initiation and propagation in the tablets (regime 3) for high values of Σ_i.

The last two regimes lead to an overall brittle behavior of the RVE and are not desirable while the first regime is characterized by interface crack propagation that promotes extrinsic reinforcement through mechanisms such as crack deviation or crack bridging. In addition, for regime 1 the stress does not fall to zero even after complete crack propagation (capping of the number of broken bonds in Fig. 13) due to friction

and interlocking that keep a non-zero stress level. The failure regime also depends on the overlap aspect ratio ρ_0 : small values of ρ_0 promote regime 1 while large values are associated to regime 3 (Fig. 11).

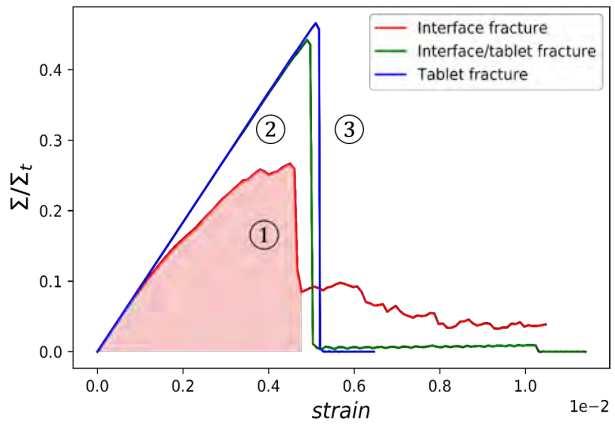

FIGURE 12: Typical stress-strain curves for Σ_i = 200 MPa ,1 200 MPa and 4 000 MPa. Three fracture regimes can be identified with increasing interface strengths Σ_i : (1) Interface fracture, (2) Interface/tablet fracture and (3) Tablet fracture.

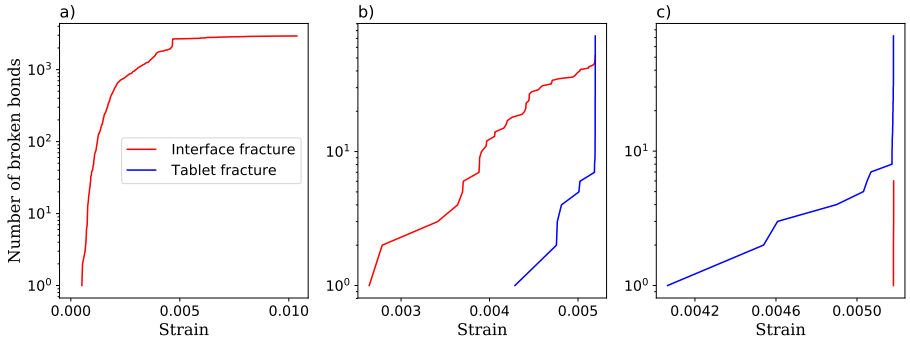

FIGURE 13: Number of broken bonds versus strain for both interface and tablet, where red and blue curves represent the interface and the tablet bonds, respectively. (a) Interface fracture initiation and propagation (b) Interface fracture initiation and tablet fracture propagation (c) Tablet fracture initiation and propagation.

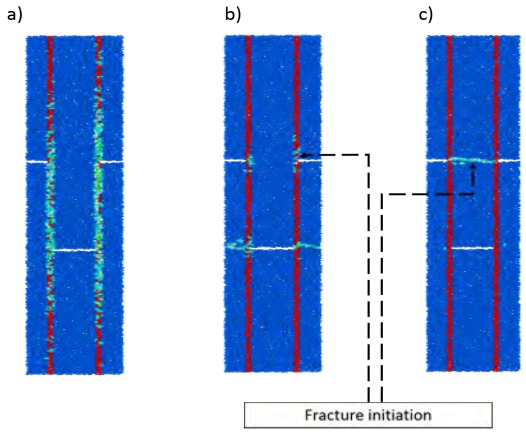

FIGURE 14: The corresponding illustrations of number of broken bonds per particle for the three cases of crack initiation and propagation. (a) Interface fracture initiation and propagation (b) Interface fracture initiation and tablet fracture propagation (c) Tablet fracture initiation and propagation.

To optimize Σ_i on a quantitative basis, the strength (maximum stress) and the dissipated energy (area under the stress-strain curve) are plotted in Fig. 15. As already mentioned, for regime 1 the stress does not fall to zero. The dissipated energy is only computed during crack propagation and does not encompass the energy dissipated by the friction of the broken interfaces after crack propagation (see highlighted area under curve 1 in Fig. 12). The value reported for regime 1 thus corresponds to a lower bound of dissipated energy as friction at broken interfaces may play a non-negligible role in alumina-nacre reinforcement. The examination of the evolution of strength and dissipated energy with increasing Σ_i shows a similar and nearly monotonic behavior that looks disappointing in terms of optimization. Although used by some authors for optimization purposes (e.g. Barthelat [2014]), dissipated energy is only a mere indicator of the material fracture toughness. It should be clear that even though they exhibit the largest dissipated energy, samples with large interface strength have a non-desirable brittle behavior, while samples under regime 1 should give rise at a larger scale to extrinsic reinforcement leading to a rising R-curve behavior with high fracture toughness (for sufficiently long cracks). A closer look at Fig. 15 and considering the three fracture regimes, show that an interesting optimal value for interface strength maybe found around $0.1\Sigma_t$: both strength and dissipated energy are quite close to the maximal values obtained for large Σ_i and the crack path is still mainly confined within the interface.

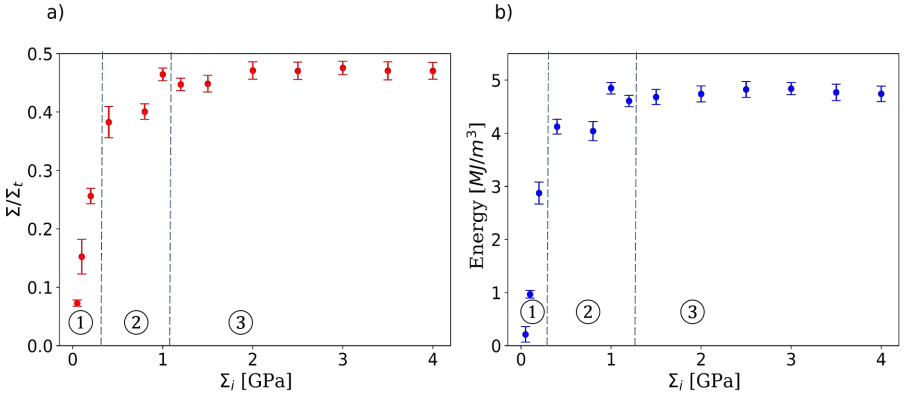

FIGURE 15: (a) Macroscopic strength and (b) fracture energy versus interface strength Σ_i. Standard deviations are calculated from five simulations. Three fracture regimes can be identified with increasing interface strengths Σ_i : (1) Interface fracture, (2) Interface/tablet fracture and (3) Tablet fracture.

The comparison with reported experimental values is also of interest. Two different interface compositions have been processed so far : Calcia/Alumina/Silica glass (Bouville et al. [2014]) and a supposedly stronger Aluminum Borate crystalline phase (Pelissari et al. [2018]). Both authors incorporated alumina nanoparticles in the interface to form strong bridges between the tablets. The reported strength values (assuming a tablet strength of 5.3 GPa, Feilden et al. [2017]) are $\frac{\Sigma}{\Sigma_t} = 0.09$ and $\frac{\Sigma}{\Sigma_t} = 0.13$, respectively. Even taking into account that strength could be overestimated by simulations at a very small scale (Roussel et al. [2016], Jauffrès et al. [2013], the comparison with simulations shows that the experimental values are still very far from the maximum strength predictions (around $\frac{\Sigma}{\Sigma_t} = 0.4$). It demonstrates that the optimal interface strength has not been reached yet and that the material can still be improved. This is consistent with the concomitant improvement in strength and toughness obtained through the use of a crystalline stronger interface as compared to the original glass interface used by Bouville et al. [2014]. The gain in strength may appear a bit low for an interface strengthening of a factor of approximately 4 (~200 MPa for aluminium borate, (Ray [1992]), versus ~50 MPa for alumina silicate glass, (Cambridge [2017]). However, one should keep in mind the detrimental effect of increasing the stiffness of the interface to a value close to the platelet's one (Fig.11). This is typically what happens when using an aluminum borate interface. The interface strength is thus a key parameter to optimize the mechanical behavior of brick and mortar materials.

6. Conclusions

In this work, a numerical model was developed to predict the mechanical response of brick and mortar materials using DEM simulations. Elastic and fracture properties of the components of brick and mortar were calibrated by taking into account the characteristics (average coordination number and packing density) of the particles packing that meshes the material. We have shown that to ensure convergence, care must be taken when choosing the number of discrete elements that mesh a material.

The comparison of our DEM simulation results to available models in the literature for a standard Representative Volume Element of a brick and mortar materials shows quite good agreement in elasticity, thus giving some confidence in the simulation results. The initiation of fracture is also in good agreement with analytical models. However, predicting fracture initiation alone fall short to model extrinsic reinforcement mechanisms that are responsible for the ability of these materials to prevent catastrophic failure. Indeed, brick and mortar materials mainly develop toughening through crack growth/propagation, after crack initiation. The added value of DEM simulations is their capability to model post-fracture behavior. Most analytical shear-lag approaches on brick and mortar materials (Barthelat [2014], Begley et al. [2012b], Ni et al. [2015]) have succeeded in predicting crack initiation but cannot investigate the crack propagation. The topological modifications (branching, bifurcation, new surface generation or crack healing) that come with fracture are indeed difficult to apprehend analytically. Even finite elements would struggle to investigate properly these discrete events. In contrast, DEM, thanks to its inherent discrete nature, is well suited for discontinuous problems.

As an application example of the proposed modeling approach, we choose nacre-like alumina, a ceramic/ceramic composite, and showed that the interface strength can be optimized to maximize strength and toughness. Three crack initiation/propagation regimes were distinguished : interface initiation and propagation (1), interface initiation followed by tablet propagation (2) and tablet initiation and propagation (3). These three regimes are governed by the ratio between the interface strength and the tablet strength. An optimal interface strength value lies at the threshold between regime (1) and (2) where the composite strength is close to its maximum value and the crack still propagates mainly within the interface, thus ensuring the development of extrinsic reinforcement and high toughness.

The geometry of the RVE used here is simple enough to allow comparison with analytical models from the literature and demonstrate the interest of the present approach to model BM materials. However, simulations at a larger scale are required to correctly assess extrinsic toughening through the propagation of cracks amid several tablet layers. This would also allow the study of the effect of material heterogeneities, e.g. in terms of overlap, tablet orientation or tablet aspect ratio. Another point that should be addressed in the future by DEM is the influence of alumina bridges between the tablets that are believed to be an essential ingredient for the exceptional mechanical performances of BM materials (Grossman et al. [2017]). Considering that DEM is based on an explicit scheme, the discrete simulations at a larger scale are anticipated to be CPU intensive. Although parallel computing is available with DEM, a careful strategy will be necessary for computing large scale problems with millions of particles.

In this work, both materials (interface and tablet) are considered as elastic-brittle. This is because our main interest is in alumina nacre which features porous alumina interfaces that are brittle. Adding some plasticity in the interface behavior will enlarge the domain in which a stable crack can grow without triggering brittle failure. A relatively simple and useful generalization of the model would thus be to consider plastic interactions in the interface to apply DEM to brick and mortar structures with ductile interfaces (metal or polymer). This is possible as DEM is also well suited for tackling plastic deformations (Martin et al. [2003], Martin [2004]).

Acknowledgements
The Agence Nationale pour la Recherche (ANR -16- CE08-0006 BICUIT, program DS0303-2016) and the AGIR-POLE-PEM 2016 project (OMicroN) are greatly acknowledged for their financial support.

References

Abid, N., Mirkhalaf, M., Barthelat, F., 2018. Discrete-element modeling of nacre-like materials : Effects of random microstructures on strain localization and mechanical performance. Journal of the Mechanics and Physics of Solids 112, 385–402.
URL https://doi.org/10.1016/j.jmps.2017.11.003

Agnolin, I., Roux, J. N., 2007. Internal states of model isotropic granular packings. I. Assembling process, geometry, and contact networks. Physical Review E - Statistical, Nonlinear, and Soft Matter Physics 76, 061302.

André, D., Iordanoff, I., Charles, J.-l., Néauport, J., 2012. Discrete element method to simulate continuous material by using the cohesive beam model. Computer Methods in Applied Mechanics and Engineering 213-216, 113–125.
URL http://www.sciencedirect.com/science/article/pii/S0045782511003811%5Cnhttp://linkinghub.elsevier.com/retrieve/pii/S0045782511003811

André, D., Jebahi, M., Iordanoff, I., Charles, J.-l., Néauport, J., 2013. Using the discrete element method to simulate brittle fracture in the indentation of a silica glass with a blunt indenter. Computer Methods in Applied Mechanics and Engineering 265, 136–147.
URL http://linkinghub.elsevier.com/retrieve/pii/S0045782513001606

Barthelat, F., 2014. Designing nacre-like materials for simultaneous stiffness, strength and toughness : Optimum materials, composition, microstructure and size. Journal of the Mechanics and Physics of Solids.

Barthelat, F., Rabiei, R., 2011. Toughness amplification in natural composites. Journal of the Mechanics and Physics of Solids 59 (4), 829–840.
URL http://dx.doi.org/10.1016/j.jmps.2011.01.001

Barthelat, F., Yin, Z., Buehler, M. J., mar 2016. Structure and mechanics of interfaces in biological materials. Nat. Rev. Mater. 1 (4), 16007.
URL http://www.nature.com/articles/natrevmats20167

Begley, M. R., Philips, N. R., Compton, B. G., Wilbrink, D. V., Ritchie, R. O., Utz, M., 2012a. Micromechanical models to guide the development of synthetic 'brick and mortar' composites. Journal of the Mechanics and Physics of Solids 60 (8), 1545–1560.
URL http://dx.doi.org/10.1016/j.jmps.2012.03.002

Begley, M. R., Philips, N. R., Compton, B. G., Wilbrink, D. V., Ritchie, R. O., Utz, M., 2012b. Micromechanical models to guide the development of synthetic 'brick and mortar' composites. Journal of the Mechanics and Physics of Solids 60 (8), 1545–1560.
URL http://dx.doi.org/10.1016/j.jmps.2012.03.002

Bekah, S., Rabiei, R., Barthelat, F., 2012. The Micromechanics of Biological and Biomimetic Staggered Composites. Journal of Bionic Engineering 9 (4), 446–456.
URL http://dx.doi.org/10.1016/S1672-6529(11)60145-5

Bertoldi, K., Bigoni, D., Drugan, W. J., 2008. Nacre : An orthotropic and bimodular elastic material. Composites Science and Technology 68 (6), 1363–1375.

Bouville, F., Maire, E., Meille, S., Van De Moortèle, B., Stevenson, A. J., Deville, S., 2014. Strong, tough and stiff bioinspired ceramics from brittle constituents. Nature Materials 13 (5), 508–514.

Cambridge, M. G. D., 2017. Ces edupack database.

Carmona, H. A., Wittel, F. K., Kun, F., Herrmann, H. J., 2008. Fragmentation processes in impact of spheres. Physical Review E - Statistical, Nonlinear, and Soft Matter Physics 77 (5), 1–10.

Chareyre, B., 2019. The Discrete Element Method for Granular Solids.

Chen, P.-Y., Lin, a. Y. M., Lin, Y.-S., Seki, Y., Stokes, a. G., Peyras, J., Olevsky, E. a., Meyers, M. A., McKittrick, J., jul 2008. Structure and mechanical properties of selected biological materials. J. Mech. Behav. Biomed. Mater. 1 (3), 208–26.
URL http://www.ncbi.nlm.nih.gov/pubmed/19627786

Christoffersen, J., Mehrabadi, M. M., Nemat-Nasser, S., 1981. A Micromechanical Description of Granular Material Behavior. Journal of Applied Mechanics 48 (2), 339.
URL http://appliedmechanics.asmedigitalcollection.asme.org/article.aspx?articleid=1405787

Corni, I., Harvey, T. J., Wharton, J. A., Stokes, K. R., Walsh, F. C., Wood, R. J. K., 2012. A review of experimental techniques to produce a nacre-like structure. Bioinspiration & Biomimetics 7 (3), 031001.
URL http://stacks.iop.org/1748-3190/7/i=3/a=031001?key=crossref.e3a5c05236625e24a3a380b558e9c9ce

Cundall, P. A., Strack, O. D. L., 1979. A discrete numerical model for granular assemblies. Géotechnique 29 (1), 47–65.
URL http://www.icevirtuallibrary.com/doi/10.1680/geot.1979.29.1.47

Dubois, F., Radjai, F., 2011. Discrete-element Modeling of Granular Materials.

Espinosa, H. D., Rim, J. E., Barthelat, F., Buehler, M. J., 2009. Merger of structure and material in nacre and bone - Perspectives on de novo biomimetic materials. Progress in Materials Science 54 (8), 1059–1100.
URL http://dx.doi.org/10.1016/j.pmatsci.2009.05.001

Feilden, E., Giovannini, T., Ni, N., Ferraro, C., Saiz, E., Vandeperre, L., Giuliani, F., 2017. Micromechanical strength of individual Al2O3 platelets. Scripta Materialia 131, 55–58.
URL http://linkinghub.elsevier.com/retrieve/pii/S1359646217300088

Grossman, M., Bouville, F., Erni, F., Masania, K., Libanori, R., Studart, A. R., 2017. Mineral Nano-Interconnectivity Stiffens and Toughens Nacre-like Composite Materials, 1–7.

Jackson, A. P., Vincent, J. F. V., Turner, R. M., 1988. The Mechanical Design of Nacre. Proceedings of the Royal Society B : Biological Sciences 234 (1277), 415–440.
URL http://rspb.royalsocietypublishing.org/cgi/doi/10.1098/rspb.1988.0056

Jauffrès, D., Liu, X., Martin, C. L., 2013. Tensile strength and toughness of partially sintered ceramics using discrete element simulations. Engineering Fracture Mechanics 103, 132–140.

Jauffrès, D., Martin, C. L., Lichtner, A., Bordia, R. K., 2012. Simulation of the toughness of partially sintered ceramics with realistic microstructures. Acta Materialia 60 (12), 4685–4694.

Jerier, J. F., Molinari, J. F., 2012. Normal contact between rough surfaces by the Discrete Element Method. Tribology International 47, 1–8.
URL http://dx.doi.org/10.1016/j.triboint.2011.08.016

Ji, B., Gao, H., 2004. Mechanical properties of nanostructure of biological materials. Journal of the Mechanics and Physics of Solids 52 (9), 1963–1990.

Katti, K. S., Katti, D. R., Pradhan, S. M., Bhosle, A., 2005. Platelet interlocks are the key to toughness and strength in nacre. Journal of Materials Research 20 (05), 1097–1100.

Kumar, R., Rommel, S., Jauffrès, D., Lhuissier, P., Martin, C. L., 2016. Effect of packing characteristics on the discrete element simulation of elasticity and buckling. International Journal of Mechanical Sciences 110, 14–21.

Launey, M. E., Ritchie, R. O., 2009. On the fracture toughness of advanced materials. Advanced Materials 21 (20), 2103–2110.

Le Ferrand, H., Bouville, F., Niebel, T. P., Studart, A. R., sep 2015. Magnetically assisted slip casting of bioinspired heterogeneous composites. Nat. Mater. 14 (September), 1–17.
URL http://www.nature.com/doifinder/10.1038/nmat4419

Le Ferrand, H., Bouville, F., Studart, A., 2018. Design principles for textured multilayered composites using magnetically assisted slip casting. arXiv :1808.01327, 1–20.

Leclerc, W., Haddad, H., Guessasma, M., 2016. On the suitability of a Discrete Element Method to simulate cracks initiation and propagation in heterogeneous media. International Journal of Solids and Structures.
URL http://linkinghub.elsevier.com/retrieve/pii/S0020768316303444

Leclerc, W., Haddad, H., Guessasma, M., 2017. International Journal of Solids and Structures On the suitability of a Discrete Element Method to simulate cracks initiation and propagation in heterogeneous media 108, 98–114.

Maheo, L., Dau, F., André, D., Charles, J. L., Iordanoff, I., 2015. A promising way to model cracks in composite using Discrete Element Method. Composites Part B : Engineering 71, 193–202.
URL http://dx.doi.org/10.1016/j.compositesb.2014.11.032

Martin, C., Bouvard, D., Shima, S., 2003. Study of particle rearrangement during powder compaction by the Discrete Element Method. Journal of the Mechanics and Physics of Solids 51, 667–693.

Martin, C. L., 2004. Elasticity, fracture and yielding of cold compacted metal powders. J. Mech. Phys. Solids 52, 1691–1717.

Martin, C. L., Bordia, R. K., 2008. Influence of adhesion and friction on the geometry of packings of spherical particles. Phys. Rev. E 77, 31307.

Ni, Y., Song, Z., Jiang, H., Yu, S. H., He, L., 2015. Optimization design of strong and tough nacreous nanocomposites through tuning characteristic lengths. Journal of the Mechanics and Physics of Solids 81, 41–57.
URL http://dx.doi.org/10.1016/j.jmps.2015.04.013

Pelissari, P. I., Bouville, F., Pandolfelli, V. C., Carnelli, D., Giuliani, F., Luz, A. P., Saiz, E., Studart, A. R., apr 2018. Nacre-like ceramic refractories for high temperature applications. J. Eur. Ceram. Soc. 38 (4), 2186–2193.
URL http://dx.doi.org/10.1016/j.jeurceramsoc.2017.10.042http://linkinghub.elsevier.com/retrieve/pii/S0955221917307227

Potyondy, D. O., Cundall, P. A., 2004. A bonded-particle model for rock 41, 1329–1364.

Ray, S. P., 1992. Preparation and Characterization of Aluminum Borate. Journal of the American Ceramic Society 75 (9), 2605–2609.

Roussel, D., Lichtner, A., Jauffrès, D., Villanova, J., Bordia, R. K., Martin, C. L., 2016. Strength of hierarchically porous ceramics : Discrete simulations on X-ray nanotomography images. Scripta Materialia 113, 250–253.
URL http://dx.doi.org/10.1016/j.scriptamat.2015.11.015

Scholtès, L., Donzé, F.-V., 2 2013. A DEM model for soft and hard rocks : Role of grain interlocking on strength. Journal of the Mechanics and Physics of Solids 61 (2), 352–369.
URL https://www.sciencedirect.com/science/article/pii/S0022509612002268

Sen, D., Buehler, M. J., 2011. Structural hierarchies define toughness and defect-tolerance despite simple and mechanically inferior brittle building blocks. Scientific Reports 1, 1–9.

Shao, Y., Zhao, H. P., Feng, X. Q., Gao, H., 2012. Discontinuous crack-bridging model for fracture toughness analysis of nacre. Journal of the Mechanics and Physics of Solids 60 (8), 1400–1419.
URL http://dx.doi.org/10.1016/j.jmps.2012.04.011

Song, Z. Q., Ni, Y., Peng, L. M., Liang, H. Y., He, L. H., 2016. Interface failure modes explain non-monotonic size-dependent mechanical properties in bioinspired nanolaminates. Scientific Reports 6 (December 2015), 1–9.

Sun, X., Zhang, Z., Xu, Y., Zhang, Y., 2015. An elastic model for bioinspired design of carbon nanotube bundles. Acta Mechanica Sinica/Lixue Xuebao 31 (2), 205–215.

William Pro, J., Kwei Lim, R., Petzold, L. R., Utz, M., Begley, M. R., 2015. GPU-based simulations of fracture in idealized brick and mortar composites. Journal of the Mechanics and Physics of Solids 80, 68–85.
URL http://dx.doi.org/10.1016/j.jmps.2015.03.011

Zhang, W., Telle, R., Uebel, J., 2014. ScienceDirect R-curve behaviour in weak interface-toughened SiC-C laminates by discrete element modelling. Journal of the European Ceramic Society 34, 217–227.

Zhang, Z. Q., Liu, B., Huang, Y., Hwang, K. C., Gao, H., 2010. Mechanical properties of unidirectional nanocomposites with non-uniformly or randomly staggered platelet distribution. Journal of the Mechanics and Physics of Solids 58 (10), 1646–1660.

Zhao, H., Guo, L., dec 2017. Nacre-Inspired Structural Composites : Performance-Enhancement Strategy and Perspective. Adv. Mater. 29 (45), 1702903.
URL http://doi.wiley.com/10.1002/adma.201702903